

www.acsanm.org Article

# Load-Bearing Nanostructures in Composites of Chitosan with Anionic Surfactants: Implications for Programmable Mechanomaterials

Suhas Gotla, Christopher Tong, and Silvina Matysiak\*



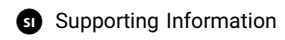
**Cite This:** ACS Appl. Nano Mater. 2022, 5, 6463–6473



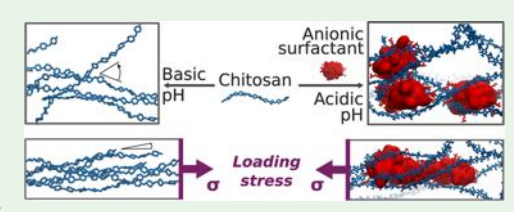
**ACCESS** I

Metrics & More

Article Recommendations



**ABSTRACT:** Polysaccharides like chitosan (CHT) can sustainably replace synthetic polymers in many material applications, but their native mechanical properties are often subpar. Addition of ionic surfactants like the anionic sodium dodecylsulfate (SDS) can bring about dramatic mechanical enhancements in polysaccharide materials, including those of CHT. At basic pH, CHT is neutral and forms elastic hydrogels, but the cationic nature of CHT at acidic pH enables ionic cross-linking with SDS, leading to viscoelastic hydrogels with superior



strength. Thus, SDS:CHT has emerged as a promising platform for spatial and dynamic programming of hydrogels with unique responses to mechanical loads, but the nanoscale origins of their load-bearing mechanisms remain elusive. To address this gap, CHT hydrogel networks were self-assembled at varying pH values and SDS concentrations and mechanically tested using a multiscale modeling pipeline. In addition to yielding self-assemblies with mechanical properties consistent with experimental reports, our methods revealed distinct pH- and SDS-dependent load-bearing mechanisms. We found that basic CHT networks underwent load-dependent crystallization, similar to stretched rubber, while SDS micelles shouldered the load response in acidic SDS:CHT networks by merging into larger micelles. These findings may enable the adaptation of these programming mechanisms for other polysaccharide—surfactant combinations, lead to the improvement of mechanical robustness of existing SDS:CHT applications, and inspire the development of new applications.

**KEYWORDS:** mechanical properties, hydrogels, biopolymers, molecular dynamics, mechanomaterials, elasticity, viscoelasticity, structure—property relationships

#### INTRODUCTION

Polysaccharides like cellulose and chitosan (CHT) are among the most abundant biomolecules found in nature. Inexpensive and biodegradable, such polysaccharides are promising alternatives to synthetic polymers for packaging, biomaterials, and other materials science applications. Yet, polysaccharides remain largely untapped as substitutes for synthetics due in large part to their underwhelming mechanical properties. 1,5–7

When used as additives, ionic surfactants can engender mechanical enhancements in polysaccharide materials. The anionic surfactant sodium dodecylsulfate (SDS) has been shown in past reports to enhance elasticity, toughness, and other properties in composite with alginate, natural gums, 9,10 CHT, 11 and other polysaccharides. 12 In the case of CHT, He et al. 11 showed that the mechanical properties of CHT hydrogels could be transformed from elastic to viscoelastic by treatment with acidic SDS solutions. In contrast to the other polysaccharide—SDS studies, He et al. also demonstrated that this acid—SDS-induced viscoelasticity could be harnessed to spatially and dynamically program the mechanical properties of CHT hydrogels, using a facile method of printing patterns with the acid—SDS solution on pre-formed basic CHT hydrogel films. While this work highlights SDS:CHT as a promising

platform for programmable mechanomaterials, their molecular and mechanistic underpinnings are not understood. Here, we aim to understand the nanoscale origins of the different mechanical properties observed in SDS:CHT hydrogels, and aid the adaptation of this programming mechanism for other polysaccharide—surfactant materials.

Toward this goal, we draw on past studies to establish the known facts and delineate the gaps in knowledge. The pH-responsive CHT is electrostatically neutral at basic pH and forms hydrogels chiefly through hydrogen bonds (H-bonds) and water bridges. <sup>13–15</sup> However, CHT is highly cationic at acidic pH (p $K_a \sim 6.5$ ), and the association of SDS with cationic CHT and similar polymers was found to be driven by electrostatics <sup>16–19</sup> and entropy. <sup>20</sup> Using scattering experiments, Hoffmann et al. deduced that ionically linked rodlike complexes are related to increased viscosity in solution phase

Received: February 6, 2022 Accepted: April 21, 2022 Published: May 4, 2022





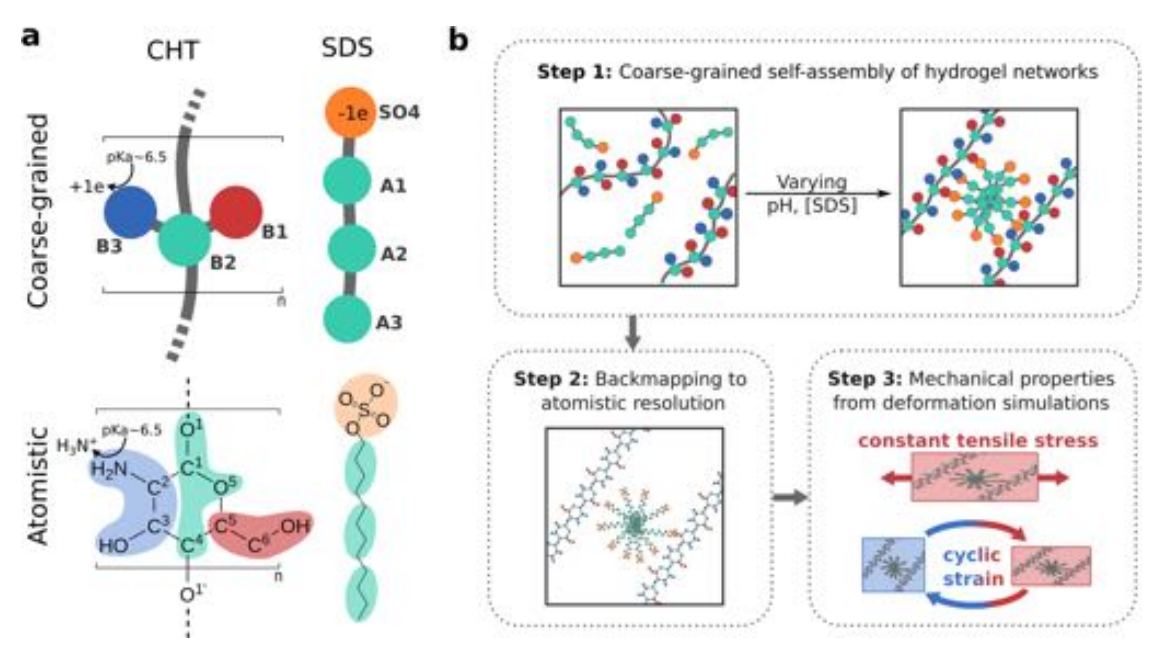


Figure 1. Overview of the multiscale modeling pipeline. (a) Coarse-grained models of chitosan (CHT) chains and sodium dodecylsulfate (SDS) surfactant molecules and their corresponding atomistic structures are shown. Protonation of the amine groups of atomistic CHT and the corresponding B3 beads of CG-CHT is dictated by the environment pH, and their inherent p $K_a \sim 6.5$ . (b) The three-step multiscale molecular modeling pipeline followed in this report is illustrated schematically.

complexes of SDS and JR 400, a polysaccharide bearing some similarities to CHT, 12 but whether these results apply to solid hydrogels is not clear. Despite the utility of scattering experiments in observing dynamic changes in molecular structure along with mechanical properties, fine nanometer length-scale resolutions (<10 nm) remain inaccessible. On the other hand, atomic force microscopy (AFM) experiments can measure mechanical moduli while simultaneously generating detailed molecular structures at <10 nm resolutions. For example, AFM has been used to explore structure-mechanical property relationships in dry cast CHT films, 21 as well as the complex formation of anionic surfactants with polycations.<sup>22</sup> However, to the best of our knowledge, AFM has not been used to investigate structure-mechanical property relationships in SDS:CHT or similar polysaccharide-surfactant hydrogels.

Molecular dynamics (MD) can be a viable computational alternative for testing mechanical properties in tandem with molecular phenomena in fine timescales and atomic detail when the molecular structure is known, <sup>23,24</sup> but the investigation of nondeterministic hydrogel structures is difficult. As a result of the complex self-assembly kinetics of hydrogels, their study with atomistic MD has been limited to early kinetic stages in small and unpercolated complexes. <sup>15,19</sup> While coarse-grained (CG) modeling (whereby atoms are grouped into "beads") curtails this challenge and allows for computationally efficient self-assembly of larger percolated hydrogel-like networks, <sup>25,26</sup> the trade-offs inherent to CG modeling yield lower resolution details vis-à-vis atomistic models.

In light of these challenges, we have combined the strengths of CG and atomistic MD to devise a three-step computational approach to develop a unified understanding of the mechanical properties and nanoscale structural dynamics in SDS:CHT hydrogels. First, percolated CHT networks at different pH and SDS concentrations were self-assembled at CG resolution, then

refined to atomistic resolution, and finally, mechanically tested in silico to gain a unified understanding of the mechanical properties and nanoscale structural dynamics (Figure 1b). In agreement with experiments, distinct pH- and SDS concentration-dependent self-assembly modes, cross-linking mechanisms, and corresponding mechanical properties were observed. Importantly, we contrast the nanoscale load-bearing mechanisms underlying the programmable mechanical properties in CHT hydrogels in the pH–SDS space. These results could assist in enhancing the robustness of the existing SDS:CHT applications<sup>27–30</sup> and enable the discovery of new applications. Furthermore, this work presents a transferrable protocol for the "full-stack" evaluation of hydrogels from self-assembly to mechanical properties, marking a significant advancement toward computational materiomics.

#### **■** METHODS

**CG Models for CHT and SDS.** Figure 1a illustrates our CG mapping, where approximately four heavy atoms are grouped into a single CG bead. In this paper, we consider the idealized case where 100% of the monosaccharide units in CHT are deacetylated. Accordingly, each CHT chain is modeled as a linear polymer of 30 N-glucosamine units, translating to a contour length of about 16 nm. N-Glucosamine units are represented by three CG beads: B1 constituting the 6'-hydroxyl group, B2 constituting the backbone atoms involved in 4,1-glycosidic bonding, and B3 constituting the ionizable 2'-amine group. The 2'-amine in CHT ionizes with  $pK_a \sim 6.5$ , allowing solution pH to be modeled by randomly placing a charge of +1 e on a fraction of B3 beads, as dictated by the Hendersen—Hasselbalch equation. However, in the pH limits explored in this work, CHT chains are either entirely neutral or entirely cationic. Further details of this CG model for CHT can be found in our previous work.  $^{2.5}$ 

The CG model of the SDS was borrowed from the standard MARTINI forcefield:<sup>31</sup> the anionic SO4 bead carries a permanent charge of -1 e and includes the sulfate headgroup, while the hydrophobic A1, A2, and A3 beads represent the hydrocarbon tail (Figure 1a). The MARTINI polarizable water model<sup>32</sup> was used to

solvate our CG systems, where each CG water represents four atomistic waters. These CG water molecules have Drude-like oscillating charges that account for the polarizability of water. Monovalent ions were used to ensure charge neutrality.

**CG Self-Assembly Simulations.** CG-CHT hydrogel networks were self-assembled using molecular dynamics simulations with varying molarities of SDS and at extreme pH conditions: basic pH > 9.3 and acidic pH < 3.7, such as the conditions used to prepare composite hydrogels of SDS and CHT by He et al. <sup>11</sup> Initially, 20 CHT chains were randomly placed in a cubic periodic box with roughly 41 000 CG water molecules for an effective concentration of about 4% (m/v) CHT. The number of CG-SDS molecules ( $n_{\rm SDS}$ ) to be inserted for a target molarity ( $M_{\rm SDS}$ ) in a system with  $n_{\rm PW}$  polarizable water molecules was determined by the equation

$$n_{\rm SDS} = \frac{4 \times n_{\rm PW} \times M_{\rm SDS}}{55.5 + M_{\rm SDS}}$$

Acidic pH systems were assembled with SDS at concentrations of 0, 22, 43, 65, 86, 130, and 180 mM. As controls, basic pH systems were assembled with SDS at concentrations of 0, 86, and 180 mM. Two independent replicas were performed for all systems except CHT with 22 and 43 mM SDS at acidic pH.

The molecular dynamics engine, GROMACS version 4.5.7,33 was used to perform the CG self-assembly simulations. To obtain a randomized starting conformation, solute molecules were set to slightly repel each other, and the systems were simulated for 25 ns in the NPT ensemble. Following randomization, repulsive potentials on solute molecules were lifted. SDS and CHT were returned to their native forcefield descriptions, and monovalent counterions were inserted as required to maintain system-wide charge neutrality. Steepest descent energy minimization was performed on these starting configurations before a 2 ns NPT equilibration run with the positions of solute molecules fixed with harmonic restraints. Lastly, unrestrained self-assembly was performed for 500 ns in the NPT ensemble. Particle motion was integrated using the leapfrog algorithm at 0.010 ps time steps. Temperature was fixed at 300 K using the Nose-Hoover thermostat<sup>34</sup> with a time constant of 4 ps, and pressure was maintained at 1 bar using the Parrinello-Rahman barostat<sup>35</sup> with a time constant of 10 ps. Isotropic pressure coupling with a compressibility of 4.5  $\times$  10<sup>-6</sup> bar<sup>-1</sup> was applied. Short-range electrostatics and van der Waals interactions were calculated using the plain cutoff scheme for a distance of 2 nm. Long-range electrostatic interactions were calculated using the particle mesh Ewald<sup>36</sup> method, with a relative permittivity,  $\epsilon$ , set at 2.5. Dummy bonds of MARTINI polarizable water were constrained using the LINCS algorithm.3

Characterization of Self-Assembled Structures. To study the patterns of growth in the self-assembly of SDS:CHT hydrogels at different pH conditions and SDS concentrations, a clustering algorithm based on the principle of breadth-first search<sup>38</sup> was established. The self-contact matrix of SDS atoms was traversed every 0.1 ns to find connected components. A group of SDS molecules were said to constitute a micellar aggregate if there existed a path between them through either of their two distal hydrophobic tail beads (A2 and A3 in Figure 1a). The existence of a path was determined by a maximum bead-to-bead distance cutoff of 0.65 nm. The number of micellar aggregates and their respective aggregation numbers were computed over all trajectories.

Similarly, the self-contact matrix of CHT atoms is traversed every 0.1 ns to find connected components. In this case, a group of CHT chains are said to constitute a cluster if there exists a path between their B2 backbone beads, either by direct backbone—backbone contacts or indirectly mediated by an SDS micelle. Backbone—backbone contacts were defined as a pair of B2 backbone beads within a distance threshold of 0.55 nm. Backbone—micelle contacts exist when a CHT B2 is within 0.55 nm of an SDS headgroup bead (SO4) in the micelle (Figure 1a). If two different CHT chains are in contact with the same SDS micelle, an SDS-mediated cross-link is said to exist

between them. All distance thresholds included the first neighbor peak of their respective pair correlation functions.

CHT clusters were considered hydrogel networks if they displayed percolation along any direction in space. From visual inspection, cluster sizes of 14 and higher displayed percolation and remained stable over the final 100 ns of simulation, and thus 14 was set as the threshold to qualify as a hydrogel network. At each time step, the systems were assigned a Boolean percolation number: 1 if the cluster size is at least 14 and 0 otherwise. Fitting a logarithmic growth curve to the time series of this Boolean percolation yielded a characteristic percolation time, which corresponded to a "half-life" for percolation.

**Backmapping from CG to Atomistic Resolution.** Self-assembled CG structures were converted to high-resolution atomistic structures using the backmapping protocol developed by Wassenaar et al.<sup>39</sup>

Figure 1a illustrates the mapping of CG-CHT and CG-SDS beads to their corresponding atomistic resolution atoms. Accordingly, target atomistic topologies for all molecules were projected onto the CG structures. Notably, the 100% deacetylation degree of CHT is maintained after backmapping, such that the atomistic CHT chains are also 30-mer *N*-glucosamine chains. Each CG water represents four atomistic water molecules; <sup>32</sup> thus, four atomistic water molecules are projected onto each CG water, such that the CG-solvation structure is maintained. As CG ions are considered to be solvated ions, <sup>31</sup> they are each backmapped to one atomistic ion and four atomistic waters.

Next, the projected structures were relaxed through two steepest descent energy minimization steps, first with intermolecular interactions turned off and second with intermolecular interactions turned on. Then, with hydrogen bonds constrained and non-hydrogen solute molecules held with harmonic position restraints, the systems were relaxed with a series of five short 500 time step NVT MD simulations while gradually increasing the time step of integration from 0.1 to 2 fs. All of the MD steps were performed at a temperature of 300 K.

Following this backmapping process, solvent molecules were allowed to achieve a stable density during 2 ns of NPT simulation with position-restrained solute molecules. Finally, restraints on solute molecules were lifted, and systems were simulated until their structures reached equilibrium, indicated by a constant population over at least 15 ns of four types of intermolecular interactions:

- CHT-CHT H-bonds, defined by a distance of less than 0.3 nm between hydrogen bond acceptors (any nitrogen or oxygen) and any polar hydrogens and a maximum donorhydrogen-acceptor angle of 150°.
- SDS-CHT H-bonds, defined the same as CHT-CHT H-bonds
- CHT-CHT water bridges, considered to be present between CHT chains if a water molecule's oxygen atom is within 0.3 nm of a pair of polar atoms (any nitrogen or oxygen) of a CHT molecule.
- SDS-CHT salt bridges, defined by a distance of 0.4 nm or less between a sulfur atom of an SDS molecule and a nitrogen atom of a protonated -NH<sub>3</sub><sup>+</sup> group of a CHT molecule.

Three representative 4% CHT hydrogel networks in the pH–SDS space were selected for this analysis: 0 mM SDS at basic pH (NB-0), 180 mM SDS at basic pH (NB-180), and 180 mM SDS at acidic pH (NA-180). NB-0 and NA-180 were simulated for 25 ns and NB-180 for 35 ns.

The molecular dynamics engine, GROMACS version 4.5.7, <sup>33</sup> was used to generate the equilibrated atomistic structures. NPT production simulations were performed with a time step of 2 ps, enabled by constraining all covalent hydrogen bonds using the LINCS algorithm. <sup>37</sup> Temperature was fixed at 300 K using the Nose–Hoover thermostat <sup>34</sup> with a time constant of 1 ps, and pressure was maintained at 1 bar using the Parrinello–Rahman barostat <sup>35</sup> with a time constant of 5 ps. Isotropic pressure coupling with a compressibility of  $4.5 \times 10^{-6}$  bar <sup>-1</sup> was applied. Short-range electrostatics and van der Waals interactions were calculated using the plain cutoff scheme for a distance of 1.4 nm. The particle mesh

Ewald method was used to calculate long-range electrostatics. The carbohydrate-specific united atom forcefield, GROMOS 53a6 GLYC, <sup>40</sup> was used. All atomistic simulations used the three-site simple point-charge (SPC) water model. <sup>41</sup>

In Silico Mechanical Testing of Atomistic Structures. Constant stress uniaxial deformation was performed by applying a negative pressure,  $p_{\rm app}$ , along the deforming axis, against the positive atmospheric pressure,  $p_{\rm atm}$ , of 0.1 MPa. The net loading stress,  $\sigma_{\rm load}$ , is given by  $\sigma_{\rm load} = -(p_{\rm app} - p_{\rm atm})$ . Constant stress simulations were performed for 15 ns at varying stresses, each starting from the final frame of the preceding simulations, where backmapped atomistic structures were equilibrated. Anisotropic pressure coupling was implemented, with  $p_{\rm app}$  applied along the deforming axis and  $p_{\rm atm}$  applied along the nondeforming axes, using the Parrinello–Rahman barostat at a time constant of 5 ps<sup>35</sup> and a compressibility of 4.5  $\times$  10<sup>-6</sup> bar<sup>-1</sup> along all three axes. The final strain was considered to be reached when the 95% confidence interval for mean strain fell below 0.01 strain units over 2 ns of simulation.

Nonequilibrium molecular dynamics was implemented to perform cyclic deformations, starting from the equilibrated backmapped atomistic structures. Dimensions of the deformation axis were changed according to the function  $L(t) = L(0) + L(0) \times d\gamma/dt \times t$ , where L(0) is the initial box length before deformation, t is the time elapsed during deformation, and  $d\gamma/dt$  is the constant strain rate relative to the original box length L(0). The box length along the deformation axis was extended with a constant strain rate,  $d\gamma/dt =$ +0.01 ns<sup>-1</sup>, during the tension leg, and compressed with a constant strain rate  $d\gamma/dt = -0.01 \text{ ns}^{-1}$ . Each leg was simulated for 15 ns such that the deformation axis reached a maximum strain  $\gamma_{max}$  of 0.15 at the end of the tension leg and a minimum strain  $\gamma_{min}$  of 0 at the end of the compression leg, and a total of three consecutive cycles were performed. Pressure coupling was anisotropic, with a pressure of  $p_{\text{atm}}$ and a compressibility of  $4.5 \times 10^{-6}$  bar<sup>-1</sup> along the two nondeforming axes. Along the deforming axis, compressibility was set to 0. Uniaxial stress was computed from the negative of the pressure experienced along this axis. The Parrinello-Rahman barostat with a time constant of 5 ps was used along all axes.

#### ■ RESULTS AND DISCUSSION

**Dual Pathways of Self-Assembly in the pH–SDS Phase Space.** To investigate the structural roots of the distinct mechanical properties of CHT and SDS:CHT hydrogels, networks of each were first self-assembled at the CG resolution. Starting from randomized positions, neutral CHT under highly basic conditions (pH > 9.3) and fully cationic CHT under highly acidic conditions (pH < 3.7) were self-assembled with SDS concentrations ranging from 0 to 180 mM. Self-assemblies with percolated (space spanning) CHT networks were classified as hydrogel networks, and characteristic percolation times for hydrogel network formation are reported in Table 1. Under basic conditions, CHT formed hydrogel networks in under 6 ns, independent of SDS

Table 1. Percolation Times in Nanoseconds (ns) for CHT Networks at Varying pH Values and SDS Concentrations<sup>a</sup>

[SDS] (mM)	pH < 3.7	pH > 9.3
0	no network*	5.3*
22	no network	_
43	no network	_
65	no network*	_
86	56.5*	5.9
130	19.8*	_
180	10.4*	4.4

<sup>&</sup>quot;Asterisk signs (\*) indicate times averaged over two independent replicas, and untested conditions are indicated by a dash (-).

concentration. In stark contrast, percolated hydrogel networks emerged under acidic pH only after a critical SDS concentration was reached: hydrogel networks were only observed at SDS concentrations upwards of 86 mM; moreover, percolation times decreased as SDS concentration increased. Thus, two pathways of CHT hydrogel assembly are observed—one that is SDS-independent at basic pH and another that is strongly SDS-dependent at acidic pH.

Pair correlation functions g(r) illustrate the structural differences between hydrogel networks assembled via these two distinct self-assembly modes. Pair correlations between CHT's B2 backbone beads  $(g_{B2-B2}(r))$  and between SDS's A3 core and S04 headgroup beads  $(g_{A3-SO4}(r))$  are observed simultaneously in Figure 2 to disentangle the effects of pH and SDS (see bead definitions in Figure 1a). Figure S1 in the Supporting Information shows the temporal evolution of  $g_{B2-B2}(r)$  and  $g_{A3-SO4}(r)$ . Although percolation times at basic pH are well under 10 ns, these temporal insights show that structures continue to evolve past the percolation point. Convergence of  $g_{A3-SO4}(r)$  and  $g_{B2-B2}(r)$  under basic pH occurred at similar timescales at all SDS concentrations but varied under acidic conditions, further emphasizing the interplay between pH and SDS contents in self-assembly.

We focus on two hydrogel networks, NA-180 (network assembled under acidic pH with 180 mM SDS) and NB-180 (network assembled under basic pH) in the final 100 ns of the trajectories when both  $g_{A3-SO4}(r)$  and  $g_{B2-B2}(r)$  have reached equilibrium. Snapshots of the equilibrium structures of NB-180 and NA-180 are shown in Figure 2d,2e, respectively. In NB-180, the correlation between interchain pairs of CHT's B2 backbone beads is characterized by a high-intensity peak at  $r \sim$ 0.5 nm (roughly the van der Waals diameter of B2 beads), followed by periodic peaks of rapidly decaying intensities at longer distances (Figure 2a). The short-range peak at  $r \sim 0.5$ nm corresponds to attractive interactions between polar B2 beads, and the smaller periodic peaks at roughly 0.5 nm increments indicate that these interchain B2 pairs form ordered crystal-like domains at CHT chain junctions (Figure 2a, inset).

There were a number of key differences in NA-180, where polycationic CHT chains were ionically cross-linked to anionic SDS. As expected, the short-range attractive B2–B2 contacts at  $r \sim 0.5$  nm are eliminated by electrostatic repulsion. On the other hand, the broad peak at r of 2.0–4.0 nm corresponds to roughly double the SDS micelle radius, which is estimated to be in the 1.0–2.0 nm range from the maximum intensities in the A3–SO4 pair correlation function between core—headgroup pairs of SDS molecules (Figure 2b,c). Thus, CHT chains were ionically bridged across SDS micelles. As multiple CHT may bind to the same SDS micelles, some CHT chains may only be separated by single SO4 headgroups—this type of binding corresponds to the intensity at  $r \sim 1.0$  nm (approximately double the van der Waals diameter of the CG beads).

Comparison with Experiments. SDS-independent self-assembly at basic pH and SDS-dependent self-assembly at acidic pH were also observed by He et al., who demonstrated that SDS was immobilized within CHT hydrogels at acidic pH but could be easily washed away at basic pH.<sup>11</sup> Our observation that percolated hydrogel networks of cationic CHT require a critical concentration of SDS is also in agreement with previous publications. Using turbidity experiments, these reports showed that gel-like insoluble complexes

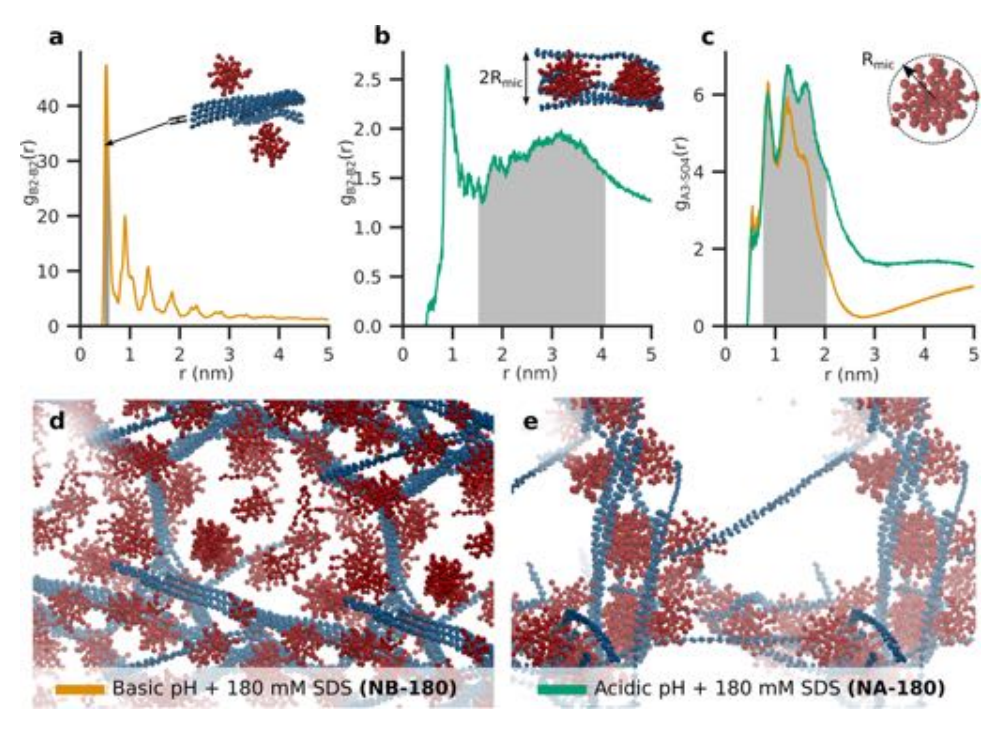


Figure 2. Effect of pH on the structural organization of SDS:CHT networks. (a) Pair correlation of interchain B2 backbone bead pairs,  $g_{\rm B2-B2}(r)$ , in the CHT hydrogel network with 180 mM SDS at basic pH (NB-180). The first peak at  $r \sim 0.5$  nm, highlighted with gray, corresponds to direct B2-B2 contacts, as seen in the inset. (b)  $g_{\rm B2-B2}(r)$  for CHT hydrogel with 180 mM at acidic pH (NA-180) shows the lack of direct B2-B2 contacts at  $r \sim 0.5$  nm. The broad peak at 1.5 nm < r < 4 nm highlighted in gray represents B2-B2 pairs cross-linked across SDS micelles, as shown in the inset. (c) Pair correlation between the tail bead A3 and the headgroup SO4 of SDS ( $g_{\rm A3-SO4}(r)$ ) of NA-180 and NB-180 indicates that micelles have similar radii 0.75 nm <  $R_{\rm mic} < 2$  nm, highlighted in gray, and illustrated in the inset. Data from NB-180 and NA-180 are plotted in orange and green, respectively. Pair correlations were computed over the final 100 ns of the self-assembly simulations, sampled every 1 ns. Full snapshots of CG hydrogel networks of NB-180 (d) and NA-180 (e) at the final time step of their self-assembly simulations are shown, with SDS colored in red and CHT colored in blue. The insets of panels (a)-(c) are zoomed in visualizations of structures from panels (d) and (e).

of SDS and cationic CHT were observed at and above a critical SDS concentration but not below.  $^{16,42}$ 

Furthermore, the crystal-like domains of CHT chains observed in the hydrogel networks at basic pH (NB-180 in Figure 2a,d) and the lack thereof at acidic pH (NA-180 in Figure 2b,e) are validated by experimental studies: it was found using X-ray diffraction that characteristic signatures for Hbonding in crystalline domains of CHT were present in gels assembled at basic pH but were lost in acidic SDS:CHT gels.<sup>43</sup> The rodlike structural organization of SDS:CHT complexes within the hydrogel network at acidic pH (inset of Figure 2b) is similar to that observed for SDS and the cationic polysaccharide JR 400 by Hoffmann et al. by scattering experiments. 12 Hoffmann et al. describe the complex as having a core composed of only surfactants, a mixed layer where polysaccharide JR 400 is interpenetrated within the surfactant micelle, and an outer layer composed of only JR 400. JR 400 contains bulky hydrophobic side chains, which may penetrate the hydrophobic surfactant core, while the 100% deacetylated CHT used in these simulations does not have any hydrophobic side chains, thus reducing the likelihood of observing CHT within the hydrophobic core of the SDS. Accordingly, we observe rodlike complexes with cores composed of only SDS and shells composed of only CHT but not an interpenetrated layer of SDS-CHT.

Backmapping to Atomistic Resolution Reveals pH-Dependent Cross-Link Populations and Thermodynamic Insights. Relative to atomistic-scale simulations, CG resolutions enable more efficient sampling of kinetic processes, like hydrogel self-assembly, but limit structural detail to atom groups. Backmapping to atomistic resolution allows us to recover the detailed atomic structures from CG assemblies. Percolated networks NA-180, NB-180, and NB-0 (CHT hydrogel network at basic pH with 0 mM SDS) were backmapped to observe atomistic structural differences of CHT hydrogels assembled in the pH–SDS space. The crystalline association of CHT chains at basic pH is clearly visible in the snapshots of the NB-0 and NB-180 assemblies (Figure 3a,b). The snapshot of NA-180 shows the lack of such crystalline associations; rather, CHT chains were primarily bridged across SDS micelles (Figure 3c) forming a network of rodlike complexes similar to those observed by Hoffmann et al. 12,44

Quantitative analysis of the populations of four different intermolecular interaction types in NB-0, NB-180, and NA-180 reveals pH-specific cross-linking patterns (Figure 3d-f). Mean populations of intermolecular CHT-CHT H-bonds and CHT-CHT water bridges under basic pH in NB-180 and NB-0 were comparable, suggesting that crystalline junctions of CHT chains are unaffected by SDS. A small population of SDS-CHT H-bonds arose from the superficial binding of some SDS micelles with neutral CHT chains in NB-180, where CHT's polar hydrogens served as H-bond donors to SDS's polar oxygens. Visual examination revealed that SDS micelles did not take part in cross-linking between H-chains (Figure 3b). In contrast, the population of CHT-CHT H-bonds was negligible in NA-180, and CHT-CHT water bridges were present in reduced amounts compared to the basic pH systems.

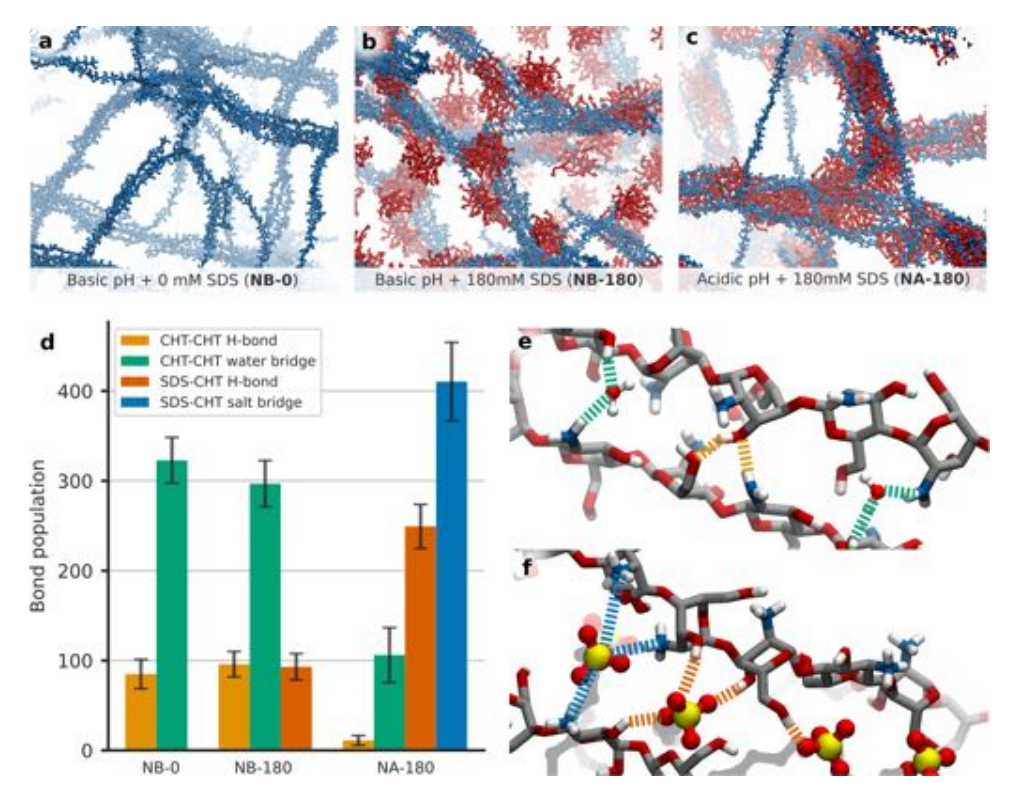
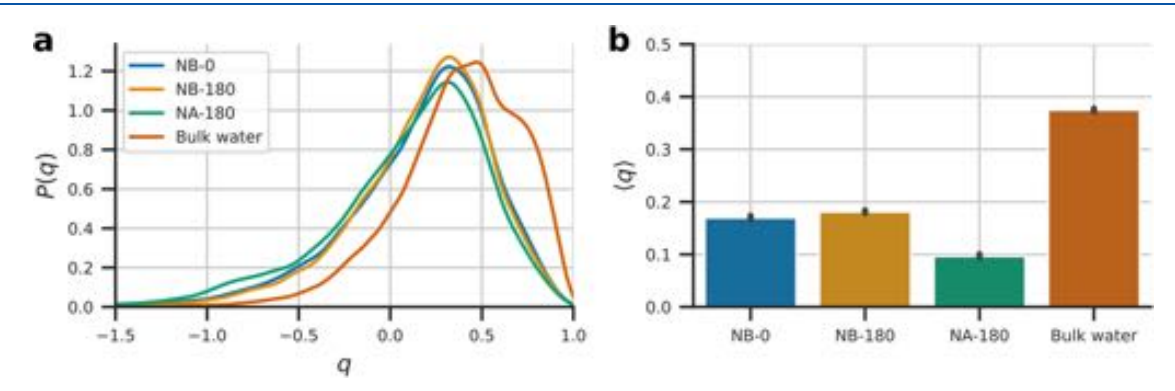


Figure 3. Characterization of physical cross-linking in backmapped hydrogel networks. (a–c) Snapshots of equilibrium atomistic structures of NB-0, NB-180, and NA-180. (d) Mean populations of intermolecular physical bonds in NB-0, NB-180, and NA-180. Error bars indicate the 95% confidence interval of mean bond populations over the last 15 ns of simulation. (e) Snapshots of CHT–CHT hydrogen bonds (yellow) and CHT–CHT water bridges (teal). (f) Snapshots of SDS–CHT salt bridges (blue) and SDS–CHT H-bonds (orange).



**Figure 4.** Orientational order in the solvation shells of atomistic hydrogel networks. (a) Probability distributions of the orientational order parameter, q, and (b) mean orientational order parameter values  $\langle q \rangle$  for NB-0, NB-180, NA-180, and bulk water. Data are sampled over 15 ns of simulation, and error bars indicate the standard error of mean.

To gain a thermodynamic understanding of these pH-dependent cross-linking bond populations, we compared the ordering of water in the solvation shells against bulk water using the orientational order parameter, q, where the ensemble average value,  $\langle q \rangle = 1$  for perfect tetrahedral H-bond networks in hexagonal water ice, and  $\langle q \rangle = 0$  for randomly ordered molecules, such as those of ideal gases. The orientational order parameter for a water oxygen atom (OW) i,  $q_i$ , is given by

$$q_i = 1 - \frac{3}{8} \sum_{j=1}^{3} \sum_{k=j+1}^{4} \left( \cos(\psi_{jik}) + \frac{1}{3} \right)^2$$

where the angle  $\psi_{jik}$  is formed by the original  $OW_i$  atom and the nearest-neighbor atoms  $OW_j$  and  $OW_k$   $(j, k \le 4)$  with  $OW_i$  at the apex.

We defined the first solvation shell by finding the OW atoms within 0.35 nm of our hydrogel solutes, CHT and SDS. Then, we found *q* for each OW in the first hydration shell by finding the four nearest OW atoms. To compare the solvation shell with bulk water, we simulated about 4000 SPC water molecules with NPT molecular dynamics for 60 ns, following the same protocol used for the simulation of the atomistic hydrogel networks NB-0, NB-180, and NA-180. The orientational order analysis was performed for the last 15 ns of simulation for bulk water, NB-0, NB-180, and NA-180, and the results are shown in Figure 4.

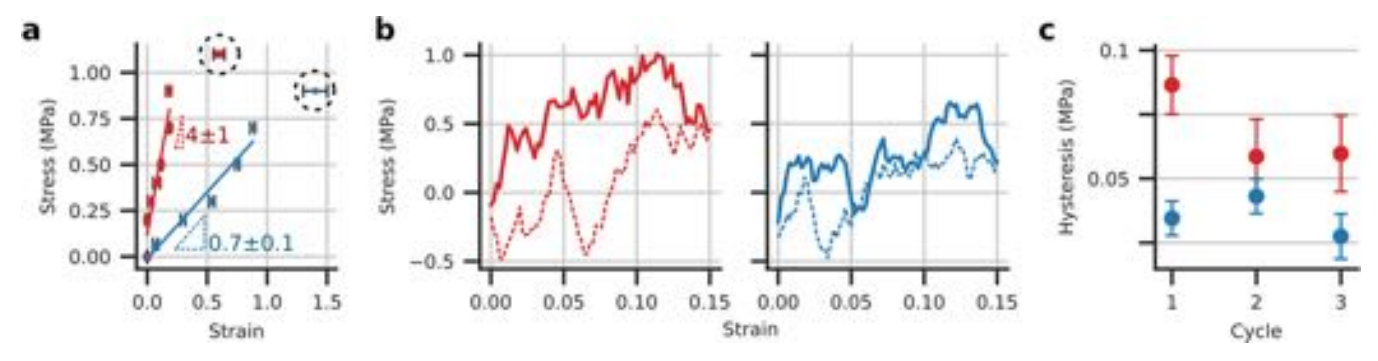


Figure 5. Mechanical characterization of NB-0 and NA-180 backmapped hydrogel networks. Data for NB-0 and NA-180 are represented in blue and red, respectively, in all panels, and the color scheme is maintained henceforth. (a) Mean strain over the final 2 ns of constant stress uniaxial deformation plotted against loading stress for NA-180 in red boxes and for NB-0 in blue circles. Error bars indicate 95% confidence intervals of mean strain over the final 2 ns, sampled every 0.1 ns. Mean strains for which error exceeds 0.02 strain units, indicating yield, are marked with dotted black circles. Nonyielding stress—strain data are fitted to the linear equation  $\sigma = E \times \gamma + c$  (stress,  $\sigma$ ; strain,  $\gamma$ ; elastic modulus; E). Elastic moduli, E, computed from the fitted slopes with the 95% confidence interval of fit are  $4 \pm 1$  and  $0.7 \pm 0.1$  MPa for NA-180 and NB-0, respectively. (b) Stress measured during the first of three cycles of tension (solid lines) and compression (dotted lines) at a constant strain rate. (c) Area of hysteresis between tension and compression curves calculated by numerical integration from each cycle of deformation (red circles for NA-180 and blue circles for NB-0). Error in area is propagated from the standard error of stress measurements.

The q distribution for bulk water in Figure 4a shows two characteristic peaks at  $q \sim 0.5$  and  $\sim 0.7$ , similar to previous reports. In contrast, the q distributions for the hydrogel networks NB-0, NB-180, and NA-180 lack these characteristic peaks and instead have a broad peak at  $q \sim 0.3$ . The distributions for NB-0 and NB-180 are nearly overlapping, while NA-180 has an additional small peak at  $q \sim -0.8$ .

These differences are more clearly apparent with the mean orientational order values,  $\langle q \rangle$  (Figure 4b). The mean value for bulk water  $\langle q \rangle \sim 0.38$  is the highest of the tested systems and indicates a high degree of tetrahedral order in the hydrogen bond network, as would be expected for liquid water. NB-0 and NB-180 have significantly lower values within the range of standard error, at about  $\langle q \rangle \sim 0.18$ , suggesting that the hydration shell is less ordered than bulk water and is well conserved at basic pH, regardless of the presence of SDS. On the other hand, NA-180 has the lowest mean value at about  $\langle q \rangle \sim 0.09$ , indicating that solvent order decreased further at acidic pH. These results corroborate past computational studies by Franca et al., 14 where it was found that the orientation of water molecules was altered by electrostatic interaction with cationic monomers of CHT, resulting in a higher exchange of water molecules and increased disorder in the solvation shell relative to neutral CHT monomers. Franca et al. also associate this increased water exchange with the superior solubility of cationic CHT (CHT is cationic and soluble at acidic pH when no ionic cross-linkers are present<sup>11</sup>).

These results can be contextualized in terms of Gibbs free energy, G, which is determined by the combination of enthalpy (H) and entropy (S) as  $\Delta G = \Delta H - T\Delta S$ . A decreased solvation shell order of NA-180 and known solubility of CHT under acidic pH have two implications: (1) solvent entropy of cationic CHT will be the highest and most favorable when CHT is free in solution due to the maximization of CHT's surface area, and (2) the conformational freedom and, thus, polymer entropy will be maximized when CHT is in solution. Thus, for the Gibbs free-energy balance to favor self-assembly  $(\Delta G < 0)$  at acidic pH, enthalpic gains  $(\Delta H < 0)$  must outweigh the entropic penalties  $(\Delta S)$  incurred by the solvent and polymer. Accordingly, we conclude that gain in enthalpy due to the formation of SDS-CHT salt bridges and H-bonds drives the self-assembly of SDS:CHT hydrogels at acidic pH.

On the other hand, the entropy of self-assembly is relatively favorable for neutral CHT hydrogels, evidenced by the higher level of order in the solvation shell. From past studies, it is known that the solvation shell also stabilizes intramolecular H-bonding in neutral CHT, which favors the restricted conformational freedom and polymer entropy of CHT in states such as the crystalline junctions in our hydrogel networks NB-0 and NB-180.

Comparison with Experiments and Computation. Structural organization of CG self-assemblies is well conserved after backmapping, and experimental comparisons from the Dual Pathways of Self-Assembly in the pH–SDS Phase Space section also hold true here. Corroborating past calorimetric studies, <sup>16,47</sup> SDS–CHT salt bridges between anionic SDS headgroups and cationic CHT amine groups were the dominant intermolecular interactions in NA-180, followed closely by SDS–CHT H-bonds. X-ray diffraction experiments by Okuyama et al. <sup>13</sup> and MD simulations by Franca et al. <sup>14</sup> previously reported the coexistence of CHT–CHT H-bonds and water bridges in crystalline CHT junctions at basic pH, but the remarkably larger population of water bridges reported here suggests an enhanced role for water in the hydrogel structure.

The relatively high and well-conserved mean orientational order parameters ( $\langle q \rangle$ ), in conjunction with the high populations of CHT-CHT cross-linking bonds, and the ordered crystalline junctions observed in our basic pH hydrogel networks NB-0 and NB-180 are consistent with past reports of the entropic favorability of neutral CHT in gellike forms. 13,14,46 While Thongngam et al. 16 have shown that the formation of SDS:CHT hydrogels is exothermic, corroborating our claim that SDS:CHT self-assembly is enthalpy-driven, the entropic contributions were not investigated. Taken together with the known entropy-driven solubility of cationic CHT reported by Franca et al., 14 here we show that the enthalpically favorable self-assembly of cationic CHT with SDS is accompanied by entropic penalties, as evidenced by the low value of the mean orientational order parameter for N-180 ( $\langle q \rangle \sim 0.09$ ).

Mechanical Characterization of Self-Assembled Hydrogel Networks. The mechanical behaviors of NB-0 and NA-180 were evaluated in silico against experimental measure-

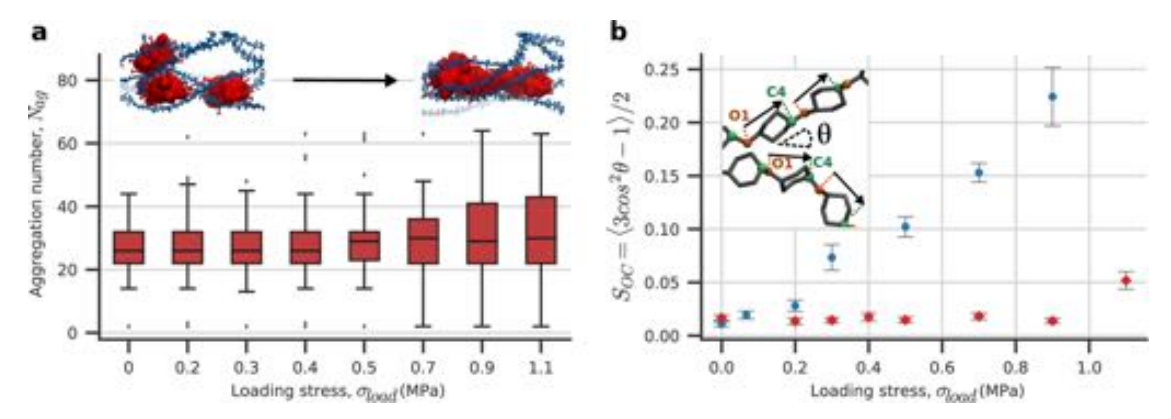


Figure 6. Molecular restructuring in response to uniaxial load from constant stress deformation. (a) Distributions of SDS aggregation numbers  $N_{\rm ag}$  in NA-180 are plotted against loading stress in the form of box-and-whisker plots. The box extends from the 25th to 75th percentile values of  $N_{\rm ag}$ . The central line represents the median or 50th percentile value. Outliers are plotted with diamond fliers. Snapshots illustrate how SDS micelles (red) merge in response to stress while cross-linking CHT chains (blue), the phenomenon responsible for the upward shift in  $N_{\rm ag}$  distributions at high loading stress. (b) Parallel ordering of the glucosamine monomers of CHT chains computed by the parameter  $S_{\rm OC} = \langle 3 \cos^2 \theta - 1 \rangle/2$ , where  $\theta$  is the angle between monomer vectors  $\overrightarrow{OC} = \overrightarrow{r_{C4}} - \overrightarrow{r_{O1}}$ , for all interchain pairs of monomers, as illustrated in the inset. Average  $S_{\rm OC}$  for NB-0 and NA-180 are plotted against loading stress in blue circles and red diamonds, respectively. Error bars represent the 95% confidence interval of the average. Data for panels (a) and (b) are gathered from the final 2 ns of constant stress deformation, sampled every 0.1 ns.

ments made by He et al. <sup>11</sup> Stress—strain curves of NA-180 and NB-0 were constructed by applying uniaxial tensile loads of increasing magnitudes and measuring the induced strain along the deforming axis  $\gamma_x = L_x(t) - L_x(0)/L_x(0)$  (Figure 5a). NA-180 and NB-0 achieved stable strains proportional to loading stresses, until the highest loads of 1.1 and 0.9 MPa, respectively, where strains displayed high variance. The high variance in strain indicates that these loading stresses exceeded the elastic limits of the hydrogel networks, causing them to undergo plastic yield. Elastic moduli were determined from the slopes of the linear elastic regions by linear regression. NA-180 and NB-0 had elastic moduli of  $4 \pm 1$  and  $0.7 \pm 0.1$  MPa, respectively.

To evaluate viscoelasticity, NA-180 and NB-0 were subjected to three cycles of tension and compression at a constant strain rate up to a maximum uniaxial strain of 15% or 0.15 strain units. Stress—strain curves obtained showed hysteresis between the tension and compression legs of the cycles in both NA-180 and NB-0 (Figure 5b). The hysteresis indicates that the stress response lags behind the strain experienced by the hydrogel networks, a definitive property of viscoelastic materials. Accordingly, the significantly higher hysteresis in NA-180 compared to that in NB-0 is indicative of a greater viscoelastic response (Figure 5c). The smaller hysteresis in NB-0 reflects the viscoelasticity inherent to CHT hydrogels.

Comparison with Experiments. The elastic moduli for acidic CHT hydrogels with SDS and basic CHT hydrogels without SDS, measured by uniaxial tension, were  $E=6.1\pm0.5$  and  $0.7\pm0.1$  MPa, respectively. While some divergence from experimental values was expected due to differences in methodology, the fitted elastic moduli  $4\pm1$  MPa for NA-180 and  $0.7\pm0.1$  MPa for NB-0 are remarkably close to the experimental values. The much higher hysteresis observed during tension—compression cycles for NA-180 compared to that for NB-0 is also in qualitative agreement with stress—strain curves generated from cyclic deformation experiments.

Further, molecular structures of NA-180 and NB-0 were analyzed in tandem with deformation. Although populations of CHT-CHT and SDS-CHT intermolecular interactions were

unaffected during both constant stress and cyclic deformations, significant restructuring was observed at the supramolecular level. Visualization of trajectories revealed enhanced restructuring of SDS micelles in NA-180 in response to uniaxial loading. Figure 6a shows the distributions of SDS aggregation numbers  $(N_{\rm ag})$ , i.e., numbers of SDS molecules within individual micelles (with  $N_{ag}$  of at least 2) over the last 2 ns of simulation. In the absence of external stress, the interquartile range (IQR) of  $N_{ag}$ , extended from 22 (Q1, the 25th percentile value) to 32 (Q3, the 75th percentile value) with a median of 26 (Q2, the 50th percentile value). IQR remained unperturbed until a loading stress of 0.7 MPa and above, where the distributions became more dispersed in proportion with stress, shifting toward higher Q3, while Q1 remained relatively stable. The upward shift is evidence of larger SDS micelles formed by merging of two or more smaller micelles, some of which have  $N_{\rm ag}$  beyond the upper fence (Q3 + 1.5 × IQR) of the distribution and represented as outliers. On the other hand, outliers below the lower fence threshold  $(Q1 - 1.5 \times IQR)$ indicate small SDS aggregates transitioning between micelles. As the IQR widened at higher stresses, such transient aggregates fell within the lower fence threshold and did not indicate an increased occurrence. Thus, external stress induces SDS to merge into larger aggregates. Under cyclic deformation, restructuring of SDS micelles was partially reversible—IQR of SDS  $N_{ag}$  increased and recovered over the first cycle but displays an upward trend with the following two cycles (Figure S2), compared to an undeformed control where  $N_{ag}$  was unchanged.

Relative alignments of CHT chains in NB-0 and NA-180 were monitored by computing the parameter  $S_{\rm OC} = \langle 3\cos^2(\theta) - 1 \rangle / 2$ , where  $\theta$  is the angle between the O1–C4 vectors of their constituent N-glucosamine monomers.  $S_{\rm OC}$ showed a pronounced increase with increasing uniaxial deformation in NB-0, demonstrating that the parallel alignment of polymers chains is enhanced and echoing the deformation-induced crystallization of polymers in a stretched rubber band. <sup>50,51</sup> On the contrary, in NA-180, there is no appreciable increase until the yielding load of 1.1 MPa. While CHT chains are the primary load-bearing components in NB-0, CHT chains in

NA-180 appear to experience significant load only during yield. Thus, the mechanical properties of NA-180 are mainly contributed by SDS micelles that restructure into larger aggregates at stresses within the linear region, and yielding occurs when the SDS domains are overwhelmed, and load is transferred to the CHT chains.

In summary, a multiscale molecular dynamics protocol was implemented to self-assemble and characterize the structure and mechanics of CHT hydrogels in the pH-SDS phase space. CG-MD was used to self-assemble percolated hydrogel networks of CHT with SDS at acidic and basic pH, from scratch, which would have been infeasible with atomistic MD due to the long timescales of kinetics and large length scales of the hydrogel systems. The CG self-assemblies, backmapped to atomistic resolution, corroborated past reports in terms of their molecular structure, 12-14,16 as well as the ordering of the solvation shell. 14,46 In addition to corroborating the enthalpic contribution to SDS:CHT self-assembly at acidic pH, 16 we showed that this process is also entropically unfavorable. Importantly, the mechanical properties of our self-assembled structures agreed closely with experimental measurements.<sup>11</sup> By observing molecular structures under mechanical stimuli, distinct mechanisms of deformation were revealed. Upon deformation, hydrogels of neutral CHT displayed enhancement in parallel alignments of CHT chains, similar to the classical example of elastic rubber bands, where stretching leads to an increase in ordered crystalline polymer junctions. 50,51 In the case of ionic SDS-CHT composites, restructuring of SDS domains cross-linking polycationic CHT was the primary structural response to loading stress, bearing resemblance with polymer gels containing hydrophobic grafts, where the mechanical properties can be tuned by the extent of hydrophobic association.

#### CONCLUSIONS

The combination of CG and atomistic molecular dynamics simulations produced nanoscale hydrogel assemblies with properties consistent with their macroscale experimental counterparts and additionally revealed key molecular phenomena underlying their mechanical behaviors, which have potential implications for a variety of programmable mechanomaterial applications. For example, strain-induced polymer crystallization could be applied to mechanically condition CHT, as done commonly with vulcanized rubber, and some polysaccharides.<sup>53</sup> The strain-induced restructuring of SDS micelles could potentially be coupled with SDS's effectiveness in encapsulating a variety of payloads, 27,29,54 similar to previously reported tensile strain-sensing membranous drug delivery systems.<sup>55</sup> These insights may also be relevant to improving the properties of food products, cosmetics, and other consumer products, where SDS:CHT and other polysaccharide-surfactant combinations are routinely used. 36,57 These findings hinge on the fundamental physical phenomena of electrostatics and hydrophobicity and may be generic to any material of similar architecture. In the same vein, the computational modeling pipeline developed is also transferrable to other systems. Together, the methods and findings described in this report contribute new insights into the load-bearing nanomechanics of CHT-SDS hydrogels with programmable mechanical properties, which may assist future efforts to adapt this programming mechanism to new applications and other polysaccharide-surfactant systems.

#### ASSOCIATED CONTENT

#### **5** Supporting Information

The Supporting Information is available free of charge at https://pubs.acs.org/doi/10.1021/acsanm.2c00560.

Figures showing the evolution of hydrogel networks in CG self-assembly simulations and evolution of SDS aggregation numbers in response to cyclic deformations (PDF)

#### AUTHOR INFORMATION

#### **Corresponding Author**

Silvina Matysiak — Fischell Department of Bioengineering, University of Maryland, College Park, Maryland 20742, United States; oorcid.org/0000-0003-3824-9787; Email: matysiak@umd.edu

#### Authors

Suhas Gotla – Fischell Department of Bioengineering, University of Maryland, College Park, Maryland 20742, United States; orcid.org/0000-0001-9035-5435

Christopher Tong — Fischell Department of Bioengineering, University of Maryland, College Park, Maryland 20742, United States; Department of Physics, Massachusetts Institute of Technology, Cambridge, Massachusetts 02139, United States; Occid.org/0000-0002-3486-4881

Complete contact information is available at: https://pubs.acs.org/10.1021/acsanm.2c00560

#### **Author Contributions**

S.G. and S.M. conceived the idea and designed the simulations for this research. C.T. contributed to the initial conception and development of methods for characterizing self-assembled structures, which were further refined and expanded by S.G. S.G. performed the simulations and analyzed the data. Interpretation of results was done jointly by S.G. and S.M. The manuscript was written by S.G. with guidance from S.M.

#### Notes

The authors declare no competing financial interest.

#### ACKNOWLEDGMENTS

This research was partially supported by the National Science Foundation under the Grant CHE-1454948 (S.G. and S.M.) and through computing resources provided by the University of Maryland. S.G.'s contribution to this research was supported, in part, by NSF award DGE-1632976. The authors would like to thank Abhilash Sahoo and Riya Samanta for providing insightful and stimulating discussions.

#### REFERENCES

- (1) Cazón, P.; Vázquez, M. Mechanical and Barrier Properties of Chitosan Combined with Other Components as Food Packaging Film. *Environ. Chem. Lett.* **2020**, *18*, 257–267.
- (2) Li, Z.; Ramay, H. R.; Hauch, K. D.; Xiao, D.; Zhang, M. Chitosan—Alginate Hybrid Scaffolds for Bone Tissue Engineering. *Biomaterials* **2005**, *26*, 3919—3928.
- (3) Li, Z.; Zhang, M. Chitosan-Alginate as Scaffolding Material for Cartilage Tissue Engineering. *J. Biomed. Mater. Res. A.* **2005**, 75A, 485–493
- (4) Fernandez, J. G.; Ingber, D. E. Manufacturing of Large-Scale Functional Objects Using Biodegradable Chitosan Bioplastic. *Macromol. Mater. Eng.* **2014**, 299, 932–938.

- (5) Reddy, M. S. B.; Ponnamma, D.; Choudhary, R.; Sadasivuni, K. K. A Comparative Review of Natural and Synthetic Biopolymer Composite Scaffolds. *Polymers* **2021**, *13*, No. 1105.
- (6) Qi, X.; Tong, X.; Pan, W.; Zeng, Q.; You, S.; Shen, J. Recent Advances in Polysaccharide-Based Adsorbents for Wastewater Treatment. *J. Cleaner Prod.* **2021**, *315*, No. 128221.
- (7) Beaumont, M.; Tran, R.; Vera, G.; Niedrist, D.; Rousset, A.; Pierre, R.; Shastri, V. P.; Forget, A. Hydrogel-Forming Algae Polysaccharides: From Seaweed to Biomedical Applications. *Biomacromolecules* **2021**, 22, 1027–1052.
- (8) Kaygusuz, H.; Evingür, G. A.; Pekcan, Ö.; von Klitzing, R.; Erim, F. B. Surfactant and Metal Ion Effects on the Mechanical Properties of Alginate Hydrogels. *Int. J. Biol. Macromol.* **2016**, *92*, 220–224.
- (9) Mithra, K.; Jena, S. S. Surfactant Head Group and Concentration Influence on Structure and Dynamics of Gellan Gum Hydrogels: Crossover from Stretched to Compressed Exponential. *J. Polym. Sci.* **2021**, *59*, 1972–1985.
- (10) Li, S.; Gao, Y.; Jiang, H.; Duan, L.; Gao, G. Tough, Sticky and Remoldable Hydrophobic Association Hydrogel Regulated by Polysaccharide and Sodium Dodecyl Sulfate as Emulsifiers. *Carbohydr. Polym.* **2018**, 201, 591–598.
- (11) He, H.; Cao, X.; Dong, H.; Ma, T.; Payne, G. F. Reversible Programing of Soft Matter with Reconfigurable Mechanical Properties. *Adv. Funct. Mater.* **2017**, *27*, No. 1605665.
- (12) Hoffmann, I.; Farago, B.; Schweins, R.; Falus, P.; Sharp, M.; Prévost, S.; Gradzielski, M. On the Mesoscopic Origins of High Viscosities in Some Polyelectrolyte-Surfactant Mixtures. *J. Chem. Phys.* **2015**, *143*, No. 074902.
- (13) Okuyama, K.; Noguchi, K.; Miyazawa, T.; Yui, T.; Ogawa, K. Molecular and Crystal Structure of Hydrated Chitosan. *Macromolecules* **1997**, *30*, 5849–5855.
- (14) Franca, E. F.; Freitas, L. C. G.; Lins, R. D. Chitosan Molecular Structure as a Function of N-acetylation. *Biopolymers* **2011**, *95*, 448–460
- (15) Morrow, B. H.; Payne, G. F.; Shen, J. pH-Responsive Self-Assembly of Polysaccharide through a Rugged Energy Landscape. *J. Am. Chem. Soc.* **2015**, *137*, 13024–13030.
- (16) Thongngam, M.; McClements, D. J. Influence of pH, Ionic Strength, and Temperature on Self-Association and Interactions of Sodium Dodecyl Sulfate in the Absence and Presence of Chitosan. *Langmuir* 2005, 21, 79–86.
- (17) Tam, K. C.; Wyn-Jones, E. Insights on Polymer Surfactant Complex Structures during the Binding of Surfactants to Polymers as Measured by Equilibrium and Structural Techniques. *Chem. Soc. Rev.* **2006**, *35*, 693–709.
- (18) Barreiro-Iglesias, R.; Alvarez-Lorenzo, C.; Concheiro, A. Chitosan/Sodium Dodecylsulfate Interactions. *J. Therm. Anal. Calorim.* **2005**, *82*, 499–505.
- (19) Tsai, C.-C.; Payne, G. F.; Shen, J. Exploring pH-Responsive, Switchable Crosslinking Mechanisms for Programming Reconfigurable Hydrogels Based on Aminopolysaccharides. *Chem. Mater.* **2018**, 30, 8597–8605.
- (20) Li, D.; Kelkar, M. S.; Wagner, N. J. Phase Behavior and Molecular Thermodynamics of Coacervation in Oppositely Charged Polyelectrolyte/Surfactant Systems: A Cationic Polymer JR 400 and Anionic Surfactant SDS Mixture. *Langmuir* 2012, 28, 10348–10362.
- (21) Luna, R.; Touhami, F.; Uddin, M.; Touhami, A. Effect of temperature and pH on nanostructural and nanomechanical properties of chitosan films. *Surf. Interfaces* **2022**, *29*, No. 101706.
- (22) Guzmán, E.; Llamas, S.; Fernández-Peña, L.; Léonforte, F.; Baghdadli, N.; Cazeneuve, C.; Ortega, F.; Rubio, R. G.; Luengo, G. S. Effect of a natural amphoteric surfactant in the bulk and adsorption behavior of polyelectrolyte-surfactant mixtures. *Colloids Surf., A* **2020**, 585, No. 124178.
- (23) Milazzo, M.; David, A.; Seob Jung, G.; Danti, S.; Buehler, M. J. Molecular Origin of Viscoelasticity in Mineralized Collagen Fibrils. *Biomater. Sci.* **2021**, *9*, 3390–3400.
- (24) Paparcone, R.; Buehler, M. J. Failure of A $\beta$ (1-40) Amyloid Fibrils under Tensile Loading. *Biomaterials* **2011**, *32*, 3367–3374.

- (25) Xu, H.; Matysiak, S. Effect of pH on Chitosan Hydrogel Polymer Network Structure. *Chem. Commun.* **2017**, *53*, 7373–7376.
- (26) Singhal, A.; Schneible, J. D.; Lilova, R. L..; Hall, C. K.; Menegatti, S.; Grafmüller, A. A Multiscale Coarse-Grained Model to Predict the Molecular Architecture and Drug Transport Properties of Modified Chitosan Hydrogels. *Soft Matter* **2020**, *16*, 10591–10610.
- (27) Pal, A.; Pan, S.; Saha, S. Synergistically Improved Adsorption of Anionic Surfactant and Crystal Violet on Chitosan Hydrogel Beads. *Chem. Eng. J.* **2013**, 217, 426–434.
- (28) Pal, P.; Pal, A. Surfactant-Modified Chitosan Beads for Cadmium Ion Adsorption. *Int. J. Biol. Macromol.* **2017**, *104*, 1548–1555.
- (29) Chatterjee, S.; Tran, H. N.; Godfred, O.-B.; Woo, S. H. Supersorption Capacity of Anionic Dye by Newer Chitosan Hydrogel Capsules via Green Surfactant Exchange Method. *ACS Sustainable Chem. Eng.* **2018**, *6*, 3604–3614.
- (30) Chekin, F.; Raoof, B.; Bagheri, J.; Abd Hamid, S. The Porous Chitosan Sodium Dodecyl Sulfate Carbon Nanotube Nanocomposite: Direct Electrochemistry and Electrocatalysis of Hemoglobin. *Anal. Methods* **2012**, *4*, 2977—2981.
- (31) Marrink, S. J.; Risselada, H. J.; Yefimov, S.; Tieleman, D. P.; de Vries, A. H. The MARTINI Force Field: Coarse Grained Model for Biomolecular Simulations. *J. Phys. Chem. B* **2007**, *111*, 7812–7824.
- (32) Yesylevskyy, S. O.; Schäfer, L. V.; Sengupta, D.; Marrink, S. J. Polarizable Water Model for the Coarse-Grained MARTINI Force Field. *PLoS Comput. Biol.* **2010**, *6*, No. e1000810.
- (33) Pronk, S.; Páll, S.; Schulz, R.; Larsson, P.; Bjelkmar, P.; Apostolov, R.; Shirts, M. R.; Smith, J. C.; Kasson, P. M.; van der Spoel, D.; Hess, B.; Lindahl, E. GROMACS 4.5: A High-Throughput and Highly Parallel Open Source Molecular Simulation Toolkit. *Bioinformatics* 2013, 29, 845–854.
- (34) Evans, D. J.; Holian, B. L. The Nose-Hoover Thermostat. *J. Chem. Phys.* **1985**, 83, 4069-4074.
- (35) Parrinello, M.; Rahman, A. Polymorphic Transitions in Single Crystals: A New Molecular Dynamics Method. *J. Appl. Phys.* **1981**, *52*, 7182–7190.
- (36) Darden, T.; York, D.; Pedersen, L. Particle Mesh Ewald: An N-log(N) Method for Ewald Sums in Large Systems. *J. Chem. Phys.* **1993**, 98, 10089–10092.
- (37) Hess, B.; Bekker, H.; Berendsen, H. J. C.; Fraaije, J. G. E. M. LINCS: A Linear Constraint Solver for Molecular Simulations. *J. Comput. Chem.* **1997**, *18*, 1463–1472.
- (38) Kozen, D. C. In *The Design and Analysis of Algorithms*; Kozen, D. C., Ed.; Texts and Monographs in Computer Science; Springer: New York, 1992; pp 19–24.
- (39) Wassenaar, T. A.; Pluhackova, K.; Böckmann, R. A.; Marrink, S. J.; Tieleman, D. P. Going Backward: A Flexible Geometric Approach to Reverse Transformation from Coarse Grained to Atomistic Models. J. Chem. Theory Comput. 2014, 10, 676–690.
- (40) Pol-Fachin, L.; Rusu, V. H.; Verli, H.; Lins, R. D. GROMOS 53A6GLYC, an Improved GROMOS Force Field for Hexopyranose-Based Carbohydrates. *J. Chem. Theory Comput.* **2012**, *8*, 4681–4690.
- (41) Mark, P.; Nilsson, L. Structure and dynamics of the TIP3P, SPC, and SPC/E water models at 298 K. J. Phys. Chem. A 2001, 105, 9954–9960.
- (42) Onesippe, C.; Lagerge, S. Study of the Complex Formation between Sodium Dodecyl Sulfate and Chitosan. *Colloids Surf., A* **2008**, 317, 100–108.
- (43) He, H.; Li, J.; Cao, X.; Ruan, C.; Feng, Q.; Dong, H.; Payne, G. F. Reversibly Reconfigurable Cross-Linking Induces Fusion of Separate Chitosan Hydrogel Films. *ACS Appl. Bio Mater.* **2018**, *1*, 1695–1704.
- (44) Hoffmann, I.; Heunemann, P.; Prévost, S.; Schweins, R.; Wagner, N. J.; Gradzielski, M. Self-Aggregation of Mixtures of Oppositely Charged Polyelectrolytes and Surfactants Studied by Rheology, Dynamic Light Scattering and Small-Angle Neutron Scattering. *Langmuir* 2011, 27, 4386–4396.

- (45) Errington, J. R.; Debenedetti, P. G. Relationship between structural order and the anomalies of liquid water. *Nature* **2001**, 409, 318–321.
- (46) Franca, E. F.; Lins, R. D.; Freitas, L. C. G.; Straatsma, T. P. Characterization of Chitin and Chitosan Molecular Structure in Aqueous Solution. *J. Chem. Theory Comput.* **2008**, *4*, 2141–2149.
- (47) Thongngam, M.; McClements, D. J. Characterization of Interactions between Chitosan and an Anionic Surfactant. *J. Agric. Food Chem.* **2004**, *52*, 987–991.
- (48) Diez-Sales, O.; Dolz, M.; Hernández, M. J.; Casanovas, A.; Herraez, M. Rheological Characterization of Chitosan Matrices: Influence of Biopolymer Concentration. *J. Appl. Polym. Sci.* **2007**, *105*, 2121–2128.
- (49) Cho, J.; Heuzey, M.-C.; Bégin, A.; Carreau, P. J. Viscoelastic Properties of Chitosan Solutions: Effect of Concentration and Ionic Strength. *J. Food Eng.* **2006**, *74*, 500–515.
- (50) Field, J. E. An X-Ray Study of the Proportion of Crystalline and Amorphous Components in Stretched Rubber. *J. Appl. Phys.* **1941**, *12*, 23–34.
- (51) Toki, S.; Fujimaki, T.; Okuyama, M. Strain-Induced Crystallization of Natural Rubber as Detected Real-Time by Wide-Angle X-ray Diffraction Technique. *Polymer* **2000**, *41*, 5423–5429.
- (52) Dompé, M.; Cedano-Serrano, F. J.; Heckert, O.; van den Heuvel, N.; van der Gucht, J.; Tran, Y.; Hourdet, D.; Creton, C.; Kamperman, M. Thermoresponsive Complex Coacervate-Based Underwater Adhesive. *Adv. Mater.* **2019**, *31*, No. 1808179.
- (53) Matsumoto, Y.; Enomoto, Y.; Kimura, S.; Iwata, T. Highly Stretchable Curdlan Hydrogels and Mechanically Strong Stretched-Dried-Gel-Films Obtained by Strain-Induced Crystallization. *Carbohydr. Polym.* **2021**, *269*, No. 118312.
- (54) Milinković Budinčić, J.; Petrović, L.; Đekić, L.; Aleksić, M.; Fraj, J.; Popović, S.; Bučko, S.; Katona, J.; Spasojević, L.; Škrbić, J.; Malenović, A. Chitosan/Sodium Dodecyl Sulfate Complexes for Microencapsulation of Vitamin E and Its Release Profile—Understanding the Effect of Anionic Surfactant. *Pharmaceuticals* **2022**, *15*, No. 54.
- (55) Jeon, H.; Kim, M. S.; Hong, S. K.; Cho, S. J.; Lim, G. Tensile Strain-Controlled Drug Delivery System Based on a Cracked Metal Structure. *Sens. Actuators, B* **2018**, *270*, 64–71.
- (56) Akanno, A.; Guzmán, E.; Ortega, F.; Rubio, R. G. Behavior of the water/vapor interface of chitosan solutions with an anionic surfactant: Effect of polymer-surfactant interactions. *Phys. Chem. Phys.* **2020**, 22, 23360–23373.
- (57) Hernández-Rivas, M.; Guzmán, E.; Fernández-Peña, L.; Akanno, A.; Greaves, A.; Léonforte, F.; Ortega, F.; Rubio, G.; Luengo, R. Deposition of Synthetic and Bio-Based Polycations onto Negatively Charged Solid Surfaces: Effect of the Polymer Cationicity, Ionic Strength, and the Addition of an Anionic Surfactant. *Colloids Interfaces* 2020, 4, No. 33.

### ☐ Recommended by ACS

## DNA-Chitosan Aerogels and Regenerated Hydrogels with Extraordinary Mechanical Properties

Irina Postnova, Yury Shchipunov, et al.

DECEMBER 18, 2021

ACS APPLIED POLYMER MATERIALS

READ 🗹

## **Protein Removal from Hydrogels through Repetitive Surface Degradation**

Tatsuki Kamiya, Akihiko Kikuchi, et al.

NOVEMBER 19, 2021

ACS APPLIED BIO MATERIALS

READ 🗹

#### Physical and Bioactive Properties of Glycosaminoglycan Hydrogels Modulated by Polymer Design Parameters and Polymer Ratio

Michael Nguyen, Alyssa Panitch, et al.

SEPTEMBER 14, 2021 BIOMACROMOLECULES

RFAD **「**へ

#### High-Performance Smart Hydrogels with Redox-Responsive Properties Inspired by Scallop Byssus

Pingping Xu, Weizhi Liu, et al.

DECEMBER 22, 2021

ACS APPLIED MATERIALS & INTERFACES

READ 🗹

Get More Suggestions >